

A modified mixed domain method for modeling acoustic wave propagation in strongly heterogeneous media

Juanjuan Gu^{a)} and Yun Jing^{b)}

Department of Mechanical and Aerospace Engineering, North Carolina State University, Raleigh, North Carolina 27695, USA

ABSTRACT:

In this paper, phase correction and amplitude compensation are introduced to a previously developed mixed domain method (MDM), which is only accurate for modeling wave propagation in weakly heterogeneous media. Multiple reflections are also incorporated with the one-way model to improve the accuracy. The resulting model is denoted as the modified mixed domain method (MMDM) and is numerically evaluated for its accuracy and efficiency using four distinct cases. It is found that the MMDM is significantly more accurate than the MDM for strongly heterogeneous media, especially when the phase aberrating layer is approximately perpendicular to the acoustic beam. Additionally, a convergence study suggests that the second-order reflection could be sufficient for cases involving high contrast inhomogeneities and large loss values (e.g., skulls). The method developed in this work could facilitate therapeutic ultrasound for treating brain-related diseases and disorders. © 2020 Acoustical Society of America.

<https://doi.org/10.1121/10.0001454>

(Received 19 November 2019; revised 17 May 2020; accepted 3 June 2020; published online 22 June 2020)

[Editor: Martin D. Verweij]

Pages: 4055–4068

I. INTRODUCTION

Numerical modeling of acoustic wave propagation in heterogeneous media is of great importance to medical ultrasound. In therapeutic ultrasound applications, for example, numerical simulations can be used to study the phase aberration in magnetic resonance (MR) imaging-guided focused ultrasound surgery^{1,2} and improve the treatment outcome. For diagnostic ultrasound, numerical modeling has been used as an important tool for image reconstruction,^{3–5} as well as to understand the sources of image degradation in ultrasound imaging.⁶

Many wave propagation algorithms that take medium heterogeneities into account have been developed. Most of these algorithms operate in the time-domain. Demi *et al.*⁷ presented an iterative nonlinear contrast source method for modeling nonlinear acoustic wave propagation in media with spatially inhomogeneous attenuation. They later extended the method to more general cases.⁸ Treeby *et al.*⁹ developed a *k*-space time-domain (KSTD) method using the coupled nonlinear wave equation. Jing *et al.*¹⁰ alternatively developed the KSTD from the Westervelt equation. Pinton *et al.*¹¹ studied a heterogeneous nonlinear attenuating full-wave model based on the finite-difference time-domain (FDTD) method. Frequency-domain methods have also been investigated. For example, Clement and Hynynen¹² combined the angular spectrum approach (ASA) with ray theory to describe the propagation of ultrasound through randomly oriented, dissipative, layered media. Vyas and Christensen¹³ modified the conventional ASA method to model linear wave propagation in inhomogeneous media.

Most recently, a mixed domain method (MDM) for modeling linear/nonlinear wave propagation in dissipative, weakly heterogeneous media has been presented.^{14,15} A detailed summary of modern ultrasound modeling algorithms can be found in a review paper.¹⁶

The present paper aims to establish and validate an accuracy-efficiency balanced numerical model for simulating acoustic wave propagation in strongly heterogeneous media. Within the realm of biomedical ultrasound, this model is particularly pertinent to transcranial ultrasound and could therefore facilitate research on high intensity focused ultrasound (HIFU) for treating brain-related diseases,^{17,18} as well as research on ultrasound-mediated neuromodulation.¹⁹ This numerical model is a nontrivial extension to the previously developed MDM,¹⁴ which is a one-way model and is only accurate for weakly heterogeneous media. To extend the original MDM to modeling wave propagation in strongly heterogeneous media, phase and amplitude corrections are proposed and evaluated in this paper. The phase correction term is first theoretically derived. As the transmission coefficient due to the variation of sound speed is not considered in the original MDM, an amplitude compensation term is also proposed. Reflections are added to the one-way model to further improve the accuracy. The resulting method is denoted the modified mixed domain method (MMDM). A one-dimensional (1D) layered medium, a two-dimensional (2D) layered medium, a 2D human skull, and a three-dimensional (3D) skull-mimicking medium are studied to evaluate the accuracy of the MMDM. A 1D analytical solution and numerical results from the MATLAB toolbox *k*-Wave²⁰ are used as the benchmark for comparison and validation purposes. The reason we chose *k*-Wave as the benchmark is that *k*-Wave is a well-established toolbox for acoustic wave simulations²⁰ and it has been used as the

^{a)}ORCID: 0000-0003-0450-6386.

^{b)}Electronic mail: yqj5201@psu.edu, ORCID: 0000-0003-2960-5292, present address: Graduate Program in Acoustics, Pennsylvania State University, University Park, Pennsylvania 16802, USA.

benchmark in our previous study.¹⁴ This study shows that the MMDM can markedly improve the results for strongly heterogeneous media in terms of the predicted waveform phase and amplitude, provided that the phase aberrating layer is approximately perpendicular to the ultrasound beam. While the addition of reflections can improve the accuracy of the model, it is also found that up to second-order reflection could be sufficient for obtaining converged results when sound absorption is considered, i.e., higher-order reflections do not significantly improve the result. This paper is structured as follows: Section II puts forward the phase correction, the amplitude compensation term, and the scheme for modeling the reflection. Section III systematically evaluates the MMDM by comparing its results with those of the analytical solution, *k*-Wave, and the MDM. Section IV discusses both the strength and weakness of the MMDM. Section V concludes the paper.

II. THEORY

A. Governing equation

We begin with the generalized Westervelt equation¹⁶ and it reads

$$\rho \nabla \left(\frac{1}{\rho} \nabla p \right) - \frac{1}{c^2} \frac{\partial^2 p}{\partial t^2} + \frac{\delta}{c^4} \frac{\partial^3 p}{\partial t^3} + \frac{\beta}{\rho c^4} \frac{\partial^2 p^2}{\partial t^2} = 0, \quad (1)$$

where p is the acoustic pressure, ρ is the ambient density, c is the speed of sound, δ is the sound diffusivity, $\delta = 2\alpha_{NP}c^3/\omega^2$ (α_{NP} is the attenuation coefficient in Np/m , and ω is the angular frequency), and β is the nonlinearity coefficient. In the original MDM, Eq. (1) would be first transformed by applying the normalized wave field $f = p/\sqrt{\rho}$, and the equation yields¹⁴

$$\nabla^2 f - \frac{1}{c^2} \frac{\partial^2 f}{\partial t^2} - f \sqrt{\rho} \nabla^2 \frac{1}{\sqrt{\rho}} + \frac{\delta}{c^4} \frac{\partial^3 f}{\partial t^3} + \frac{\beta}{\sqrt{\rho} c^4} \frac{\partial^2 f^2}{\partial t^2} = 0. \quad (2)$$

The effect of density heterogeneities is taken into account by the term $\sqrt{\rho} \nabla^2 (1/\sqrt{\rho})$. In the event that the density distribution is not sufficiently smooth, which could be the case for heterogeneous media, the Laplacian term $\nabla^2 (1/\sqrt{\rho})$ will exhibit sharp discontinuities.²¹ While this was not identified as a major issue for weakly heterogeneous media,¹⁴ it could render the algorithm unstable for strongly heterogeneous cases. A previous paper also discussed the adverse effect of this Laplacian term in the context of the KSTD method.²² Consequently, the density is first assumed to be homogeneous in the governing equation. The density heterogeneity effect will be considered later via an amplitude correction term proposed in Sec. IIC. To reduce the spatial aliasing error,²³ an absorbing boundary layer is added by introducing a frequency-independent absorption term $\gamma \partial p / \partial t$ to the governing equation,²⁴ where $\gamma = \gamma_{\max} / \cosh^2(\alpha n)$ (γ_{\max} is a constant, α is a decay factor, and n denotes the distance in the number of

grid points from the boundary). Thus, the modified governing equation reads

$$\nabla^2 p - \frac{1}{c^2} \frac{\partial^2 p}{\partial t^2} + \frac{\delta}{c^4} \frac{\partial^3 p}{\partial t^3} + \frac{\beta}{\rho c^4} \frac{\partial^2 p^2}{\partial t^2} = \gamma \frac{\partial p}{\partial t}. \quad (3)$$

This equation is akin to the original Westervelt equation, in which the sound speed c and diffusivity δ are constant with respect to the frequency. Subtracting $(1/c_0^2)(\partial^2 p / \partial t^2)$ from both sides of Eq. (3), where c_0 is a constant (generally taken as the minimum sound speed in the medium under study), and rearranging the resulting equation yields

$$\begin{aligned} \nabla^2 p - \frac{1}{c_0^2} \frac{\partial^2 p}{\partial t^2} &= \left(\frac{1}{c^2} - \frac{1}{c_0^2} \right) \frac{\partial^2 p}{\partial t^2} - \frac{\delta}{c^4} \frac{\partial^3 p}{\partial t^3} \\ &\quad - \frac{\beta}{\rho c^4} \frac{\partial^2 p^2}{\partial t^2} + \gamma \frac{\partial p}{\partial t}. \end{aligned} \quad (4)$$

By performing the Fourier transform to Eq. (4) with respect to x , y , and time t , we arrive at an equation in the frequency domain,

$$\begin{aligned} \frac{\partial^2}{\partial z^2} \tilde{P} + K^2 \tilde{P} &= F_{xy} \left\{ \left[-\frac{\omega^2}{c_0^2} \left(\frac{c_0^2}{c^2} - 1 \right) \right. \right. \\ &\quad \left. \left. + \frac{i\delta\omega^3}{c^4} + i\omega\gamma \right] F_t(p) \right\} \\ &\quad + F_{xy} \left(\frac{\beta\omega^2}{\rho c^4} F_t(p^2) \right), \end{aligned} \quad (5)$$

where \tilde{P} is the Fourier transform of p , F_{xy} is the Fourier transform operator in the x - and y -dimensions. We note that applying the Fourier transform (F_{xy}) to the terms containing the speed of sound, diffusivity, γ , and the nonlinearity coefficient in Eq. (5) mathematically gives rise to convolutions in the wave-vector domain. Our algorithm computes these convolutions by leveraging the fast Fourier transform (FFT). F_t is the Fourier transform in the time-domain, and $K^2 = \omega^2/c_0^2 - k_x^2 - k_y^2$ with k_x and k_y being the wavenumbers in the x - and y -dimensions. This equation is more general than Eq. (3) in the sense that now the speed of sound and diffusivity δ can be treated as arbitrary functions of the frequency in order to take dispersion into account.²⁵ An implicit solution to Eq. (5) is derived from the 1D Green's function in an integral form²⁵ such that

$$\tilde{P}(z) = \tilde{P}(0) e^{iKz} + \frac{e^{iKz}}{2iK} \int_0^z e^{-iKz'} M(p(z')) dz', \quad (6)$$

where

$$\begin{aligned} M(p) &= F_{xy} \left\{ \left[-\frac{\omega^2}{c_0^2} \left(\frac{c_0^2}{c^2} - 1 \right) + \frac{i\delta\omega^3}{c^4} + i\omega\gamma \right] F_t(p) \right\} \\ &\quad + F_{xy} \left(\frac{\beta\omega^2}{\rho c^4} F_t(p^2) \right). \end{aligned} \quad (7)$$

Equation (6) is solved by using a Simpson-like rule.²⁶ In this model, density, speed of sound, attenuation coefficient, power law exponent, and nonlinear coefficient can all be spatially varying functions. The Kramers-Kronig dispersion relation is applied by directly replacing the speed of sound c with c_p , and $c_p = (1/\hat{c} + \alpha_0 \tan(\pi y/2)\omega^{y-1})^{-1}$,²⁵ where \hat{c} is the sound speed at zero frequency,²⁷ y is the power law exponent, α_0 is the absorption in Np MHz^{-y} m⁻¹. The relation between α_0 and α_{NP} follows a power law, i.e., $\alpha_{NP} = \alpha_0\omega^y$. The validity of this model for accounting for absorption with an arbitrary power law was demonstrated in our earlier study using a 1D analytical solution.¹⁴ Equation (6), however, is only accurate for media with weak speed of sound contrast. As shown by our previous study,¹⁴ this model is a one-way model; it does not consider the transmission coefficient associated with the speed of sound variation. There is also an intrinsic error when computing the phase of the advancing wavefront, which grows as the speed of sound contrast increases.¹⁴ To have a more general model that could be applied to strongly heterogeneous media, phase correction and transmission compensation will be introduced. Multiple reflections are also proposed to complement the model.

B. Phase correction

Considering a 1D inhomogeneous medium with a speed of sound distribution that is

$$c = \begin{cases} c_1, & \text{when } z \leq z_0, \\ c_2, & \text{when } z > z_0. \end{cases} \quad (8)$$

The analytical solution of the pressure at $z + \Delta z$ ($z = z_0$) without considering the transmission coefficient (only consider the phase change) is

$$(P_{z+\Delta z})_{\text{analytical}} = P_z e^{iK' \Delta z}, \quad (9)$$

where K' is the wave number and $K' = \omega/c_2$, P_z is the wave pressure at z with a frequency of ω . The original MDM solution, on the other hand, is described as¹⁴

$$(P_{z+\Delta z})_{\text{MDM}} = P_z e^{iK \Delta z} + \frac{e^{iK \Delta z}}{2iK} \int_0^{\Delta z} e^{-iKz'} (M) P(z') dz'. \quad (10)$$

For 1D linear lossless wave propagation, $K = \omega/c_0$ and $M = -(\omega^2/c_0^2)(c_0^2/c^2 - 1)$. In this case, $c_0 = c_1$. It has been shown that this solution is only valid for weakly heterogeneous media.¹⁴ To solve the integral equation in the form of $y(t_{n+1}) = y(t_n) + \int_{t_n}^{t_{n+1}} f(s, y(s)) ds$, the trapezoidal rule is applied and yields

$$y_{n+1} = y_n + \frac{\Delta z}{2} [f(t_n, y_n) + f(t_{n+1}, y_{n+1})]. \quad (11)$$

Applying this to Eq. (10) leads to

$$\begin{aligned} (P_{z+\Delta z})_{\text{MDM}} &= P_z e^{iK \Delta z} \\ &+ \frac{e^{iK \Delta z}}{2iK} \frac{\Delta z}{2} [M_z P_z + M_{z+\Delta z} P_{z+\Delta z} e^{-iK \Delta z}]. \end{aligned} \quad (12)$$

By rearranging Eq. (12), we have

$$(P_{z+\Delta z})_{\text{MDM}} = \frac{P_z e^{iK \Delta z} + \frac{e^{iK \Delta z}}{4iK} M_z P_z \Delta z}{1 - \frac{M_{z+\Delta z}}{4iK} \Delta z}. \quad (13)$$

To examine the exact phase error in the MDM, Eq. (13) is subtracted from Eq. (9). Rearranging, the resulting equation yields

$$\begin{aligned} (P_{z+\Delta z})_{\text{analytical}} &= (P_{z+\Delta z})_{\text{MDM}} \\ &+ P_z e^{iK' \Delta z} \left(1 - e^{i(K-K') \Delta z} \frac{1 + \frac{M_z}{4iK} \Delta z}{1 - \frac{M_{z+\Delta z}}{4iK} \Delta z} \right). \end{aligned} \quad (14)$$

$P_z e^{iK' \Delta z} (1 - e^{i(K-K') \Delta z} (1 + (M_z/4iK) \Delta z / 1 - (M_{z+\Delta z}/4iK) \Delta z))$ is, therefore, the phase correction term. Although this correction is derived based on the 1D assumption, it can be applied to more general cases with a sufficient accuracy as shown later in this paper.

C. Amplitude compensation

The transmission coefficient due to the variation of sound speed is not considered in the original MDM, which is a significant source of error for simulations involving a large speed of sound contrast. Although the MDM could consider the transmission coefficient due to the variation of density, as stated earlier, the density heterogeneity term could introduce a singularity and render the algorithm unstable. Therefore, amplitude compensation is introduced for addressing the density and speed of sound heterogeneities. The compensation term reads (similar to what was used in Ref. 13)

$$\begin{aligned} T(x, y, z) &= \\ &\frac{2\rho(x, y, z + \Delta z) c(x, y, z + \Delta z)}{\rho(x, y, z) c(x, y, z) + \rho(x, y, z + \Delta z) c(x, y, z + \Delta z)}, \end{aligned} \quad (15)$$

where $c(x, y, z)$ and $\rho(x, y, z)$ are the speed of sound and density at plane z , respectively, and $c(x, y, z + \Delta z)$ and $\rho(x, y, z + \Delta z)$ are the speed of sound and density at plane $z + \Delta z$, respectively. Similar to Eq. (14), Eq. (15) is only exact for 1D cases.²⁸ To implement the phase and amplitude corrections, the second term on the right-hand side of Eq. (14) is added to $\tilde{P}(z)$ in Eq. (6) during the iteration for computing the integral. After applying the inverse Fourier transform to $\tilde{P}(z)$, the amplitude is then corrected by multiplying $T(x, y, z)$.

D. Multiple reflections

Reflections are further added in the MMDM by using the following equation:²⁸

$$P_{\text{reflection}} = P_{\text{incident}}(T - 1), \quad (16)$$

where P_{incident} is the incident wave used for calculating the reflected wave. For example, when calculating the first-order reflection, P_{incident} is the transmissive waveform at each plane, i.e., the result of the one-way MMDM. The corresponding $P_{\text{reflection}}$ is first calculated for each layer by Eq. (16) and stored during the forward projection step. Subsequently, the entire first-order reflection field is computed by considering $P_{\text{reflection}}$ as the boundary condition and having it propagate in the backward direction. When calculating the second-order reflection, P_{incident} is given by the first-order reflection wave field. By propagating the resulting $P_{\text{reflection}}$ in the forward direction, the second-order reflection field is formed. This procedure continues until the desired maximum order of reflection is reached. Note that the reflection coefficient ($R = T - 1$) is calculated locally based on the medium property defined at each grid point [see Eq. (15)]. This allows for the modeling of distributed scattering events rather than just scattering from layered interfaces.

In general, an even-order reflection is associated with forward propagation while an odd-order reflection travels in the backward direction. The final wave field is obtained by superposing all solutions. It is noted that, again, Eq. (16) is only exact for 1D wave propagation, which is consistent

with the assumption underpinning equations (14) and (15). A flowchart illustrating how the corrections and reflections are implemented in the MMDM can be found in Fig. 1.

III. SIMULATION RESULTS

A. Short tone bursts

For transient simulations, a Gaussian-modulated pulse is used. It is expressed as

$$p_{\text{source}} = p_0 \exp(-t^2 f_c^2 / 2) \sin(2\pi f_c t), \quad (17)$$

where p_0 is the magnitude of the pulse and f_c is the center frequency. f_c is chosen to be 700 kHz throughout this study as it is a clinically relevant frequency for transcranial ultrasound. Note that this is close to the frequency used in the mid-frequency brain system developed by InSightTec Ltd. (Haifa, Israel), which is around 670 kHz. Benchmark results are obtained by the MATLAB toolbox *k*-Wave,²⁰ except for the 1D simulation. Both spatial and temporal resolutions used in the *k*-Wave benchmark simulations are sufficiently fine in order to obtain well-converged results. L2-norm errors are calculated to quantitatively analyze the accuracy of the MMDM, and this error is defined as¹⁵

$$L2 = \frac{\|p - p_{\text{benchmark}}\|}{\|p_{\text{benchmark}}\|}, \quad (18)$$

where $\|p\|$ is the L2-norm of the acoustic pressure.

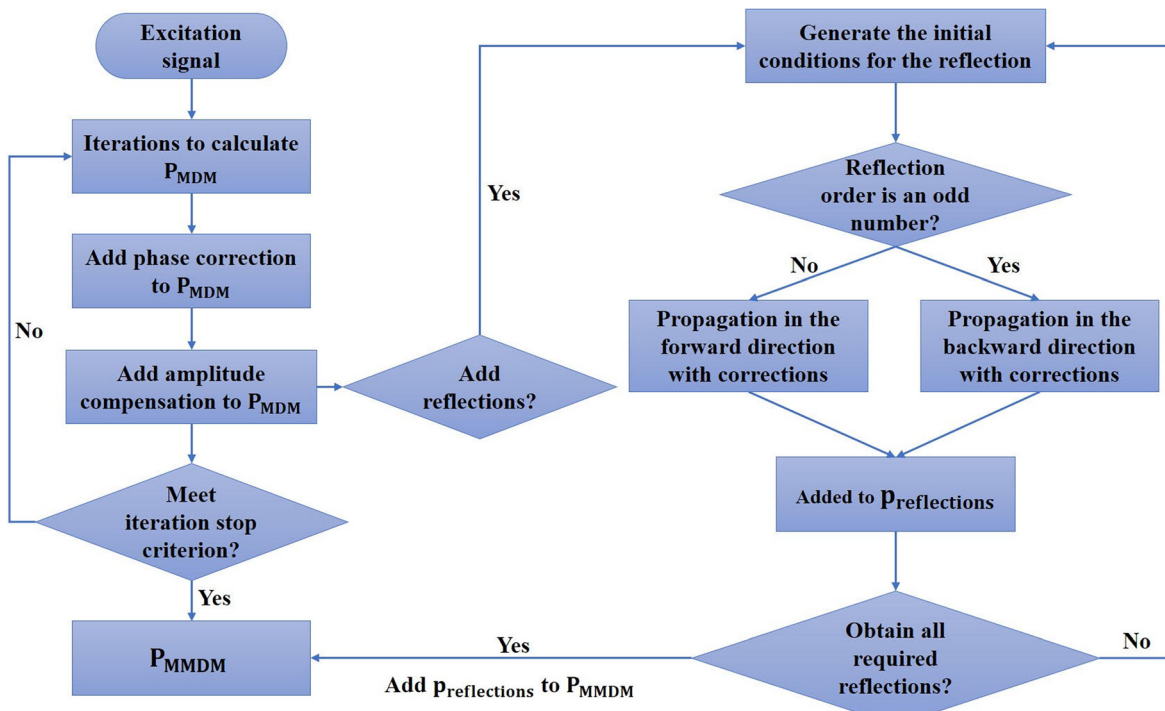


FIG. 1. (Color online) A flowchart illustrates the scheme to add corrections and reflections to the MMDM. At each iteration step, both the phase correction and amplitude compensation are added to the MDM result. For each propagation, the reflected wave field on each plane is calculated and stored. These wave fields then propagate with both phase and amplitude corrections in the forward/backward direction. The total pressure field is finally obtained by superposing the transmission and reflection wave fields.

A lossless 1D layered medium is first studied. The interlayer is 6.4 mm thick and is placed in water, in which the speed of sound and density are 1500 m/s and 1000 kg/m³, respectively. Two cases are considered. (1) The interlayer medium has a speed of sound of 3000 m/s and a density of 2000 kg/m³, indicating a contrast of 2.0; and (2) the interlayer medium has a speed of sound of 2250 m/s and a density of 1500 kg/m³, indicating a contrast of 1.5. In the MMDM simulations, 20 reflections are considered. The marching step size is varied from $\lambda/12$ to $\lambda/64$, while the temporal resolution is fixed at $1/8f_c$. λ is the wavelength in water at the center frequency f_c . The analytical solution for the intensity transmission coefficient is well known.²⁸ $T_I = 1/[1 + (1/4)(r_2/r_1 - r_1/r_2)^2 \sin(k_2 L)]$, where r_1 is the impedance of the surrounding medium, r_2 is the impedance of the interlayer medium, L is the interlayer thickness, and k_2 is the wavenumber of the interlayer medium. Figure 2(a) shows the intensity transmission coefficient as a function of frequency for the case where the contrast is 2.0 and the marching step size is $\lambda/16$. The accuracy of the MMDM is seen to decline as the frequency increases due to the fact that the marching step size becomes inadequate in capturing the rapid oscillation at higher frequencies. Figure 2(b) shows the errors for the two cases involving different contrast ratios with varying marching step sizes. L2-norm

errors are computed for the frequency range up to $4f_c$. The errors are also computed at the center frequency only. Because of the lower accuracy at higher frequencies, the L2-norm errors are larger than the errors computed at the center frequency. As expected, the error reduces as the marching step size becomes finer. Figure 2(b) additionally suggests that the stronger the inhomogeneity (contrast) is, the larger the error is. While MDM results are not included here, they will be discussed for 2D and 3D simulations. Figure 2(c) shows how the order of reflection affects the result. Here, the marching step size is $\lambda/16$, and only the errors computed for the center frequency are shown as they are of greater interest in HIFU. In both cases, it can be seen that the error stabilizes once the order of reflection is beyond four. The effect of reflection will be further discussed later for cases with higher dimensions.

A 2D layered medium shown in Fig. 3(a) is then studied. The blue region is water; in the red region, the speed of sound is 3000 m/s and the density is 2000 kg/m³, indicating a contrast of 2.0 for both acoustical properties. The transducer focal length is 68.6 mm and the transducer diameter is 34.3 mm, corresponding to an *F* number of 2.0. The pressure magnitude of the excitation p_0 is 1 Pa. The absorbing layer is enabled to minimize the spatial aliasing error. For the transient simulation, γ_{\max} is 0.6 and α is 0.05. Note that a

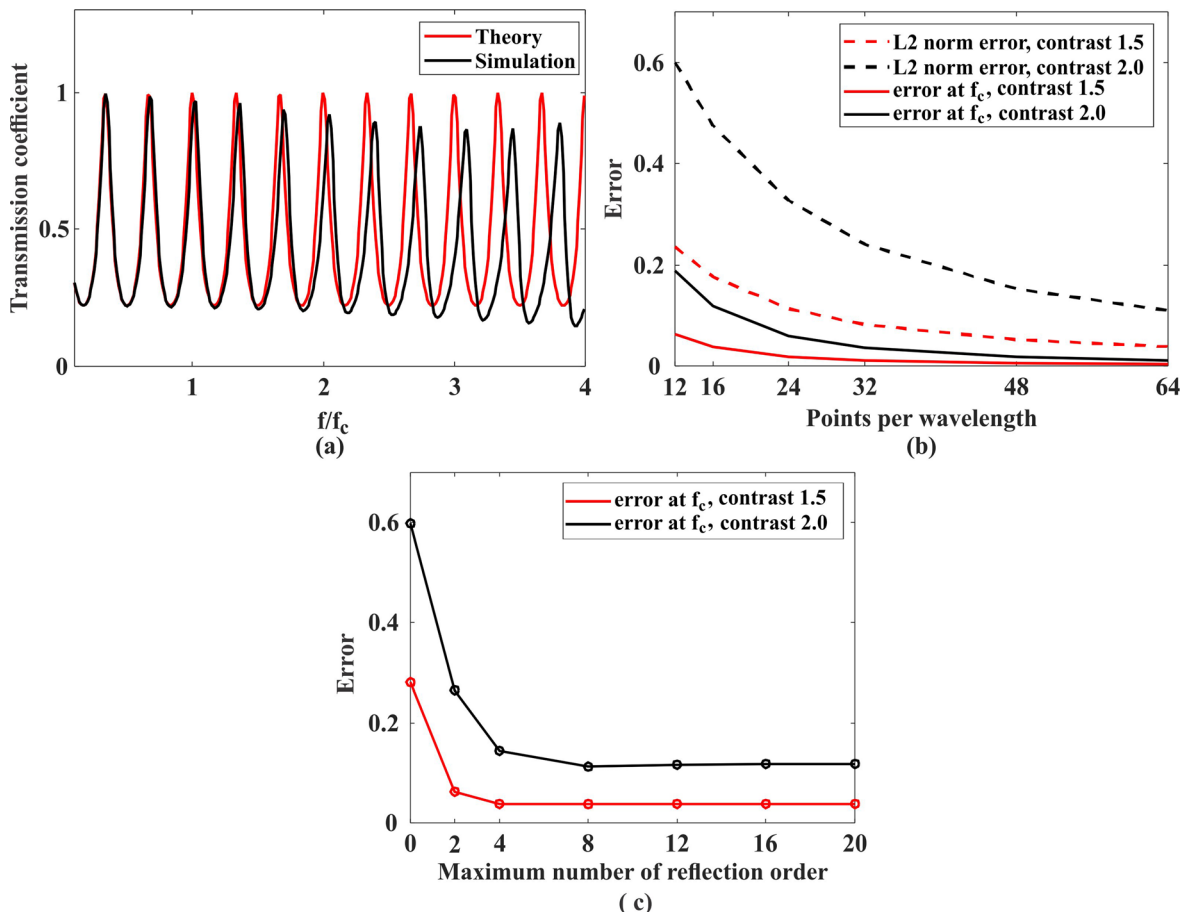


FIG. 2. (Color online) (a) Theoretically and numerically predicted intensity transmission coefficients. (b) Errors of the MMDM for various marching step sizes. (c) Error as a function on the order of reflection.

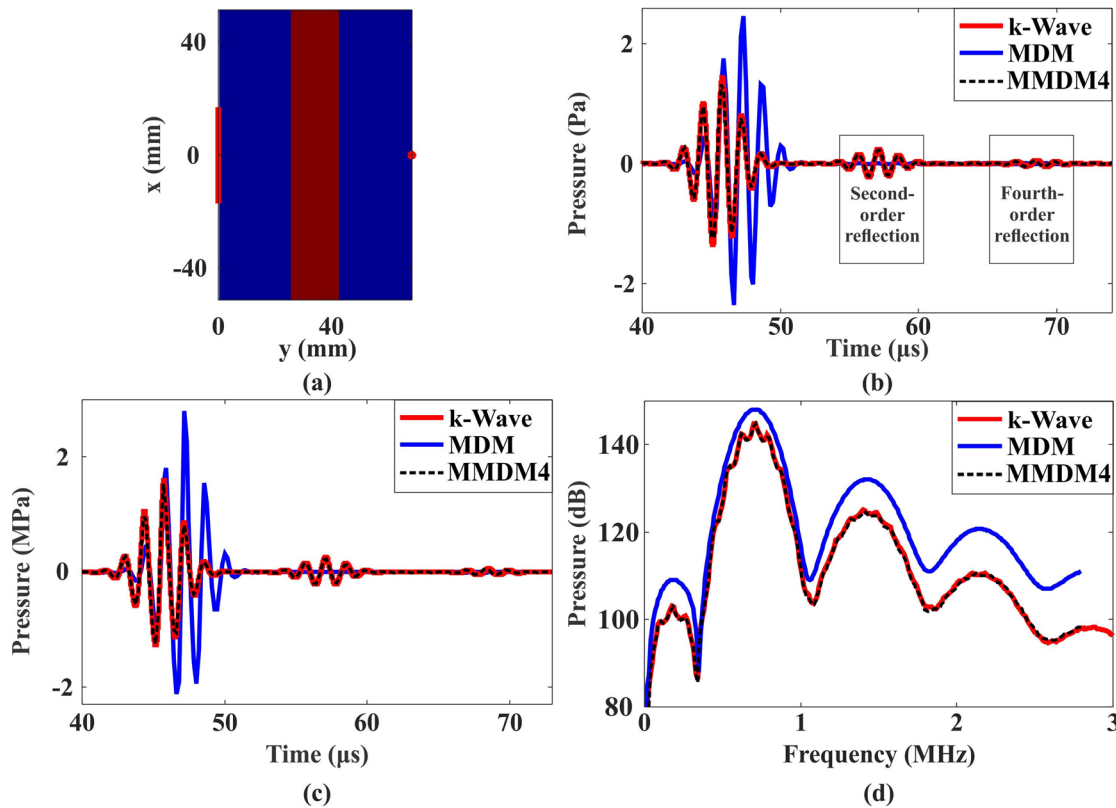


FIG. 3. (Color online) (a) A 2D layered medium. The red line indicates the phased array transducer and the red dot indicates the position of the transducer focus. (b) Waveforms recorded at the geometrical focus of the transducer. The results simulated by *k*-Wave, the MDM, and the MMDM4 are compared when the medium is linear. (c) Time-domain and (d) frequency-domain results at the geometrical focus of the transducer. The results simulated by *k*-Wave, the MDM, and the MMDM4 are compared when the nonlinear effect is considered.

large γ_{\max} or a small α implies that more energy will be absorbed by the absorbing layer, thus, reducing the spatial aliasing error (sometimes referred to as the wraparound error). On the other hand, if γ_{\max} is too large or α is too small, the algorithm could become unstable with a large step size, or the acoustic field could become inaccurate due to excess absorption. In practice, the best γ distribution yields near-zero values in the central area of the domain while the γ value increases smoothly toward the edge of the domain. More details regarding setting up the absorbing layer can be found in Ref. 24. For the benchmark simulation using *k*-Wave, the spatial step size is $1/16\lambda$. The time step size dt is $0.0045\ \mu\text{s}$, corresponding to a Courant-Friedrichs-Lowy (CFL) number of 0.1. The error of the *k*-Wave results at $\text{CFL} = 0.05$, using the results at $\text{CFL} = 0.1$ as the benchmark is on the order of 0.001, which is negligibly small when compared to the difference between the results of our algorithm and the benchmark results. The same criterion is also used to determine the spatial resolution for convergence.

For the MDM and MMDM simulations, the spatial resolution in the x direction is $1/4\ \lambda$ and it is $1/16\ \lambda$ in the y direction (marching step size). The time step size dt is $0.1786\ \mu\text{s}$. Additional simulations show that smaller dt does not significantly affect the result once the Nyquist sampling rate is well satisfied (i.e., $dt \leq 1/8f_c$). Waveforms recorded

at the transducer focus and simulated with different methods are shown and compared in Fig. 3(b). The L2-norm error is 1.2137 for the simulation with the MDM and 0.0509 for the simulation with the MMDM, incorporating up to the fourth-order reflection (denoted as MMDM4; MMDM n stands for the MMDM incorporating up to the n th-order reflection). When the nonlinearity coefficient for the whole domain is 3.6. The time-domain and frequency-domain results at the focal point are plotted in Figs. 3(c) and 3(d). The L2-norm error is 1.2234 for the MDM and 0.0579 for the MMDM4. In both linear and nonlinear cases, the error is reduced by a factor of over 20. In both Figs. 3(b) and 3(c), even-order reflections can be observed in the MMDM and *k*-Wave results as anticipated.

A 2D human skull is then studied to further validate the MMDM, and the *in silico* model is shown in Fig. 4(a). The speed of sound is between 1500 m/s and 2816.1 m/s; the density is between $1000\ \text{kg/m}^3$ and $2588\ \text{kg/m}^3$. The transducer focal length is 58.6 mm and its diameter is 39.3 mm, corresponding to an *F* number of 1.5. The pressure amplitude is 1 Pa. The spatial resolutions in the x and y directions are both 0.1953 mm (approximately $1/11\ \lambda$) for all simulations, which is determined by the computed tomography (CT) scan. The time step size in *k*-Wave is $0.0045\ \mu\text{s}$ ($\text{CFL} = 0.065$) while it is $0.1786\ \mu\text{s}$ in the MDM and

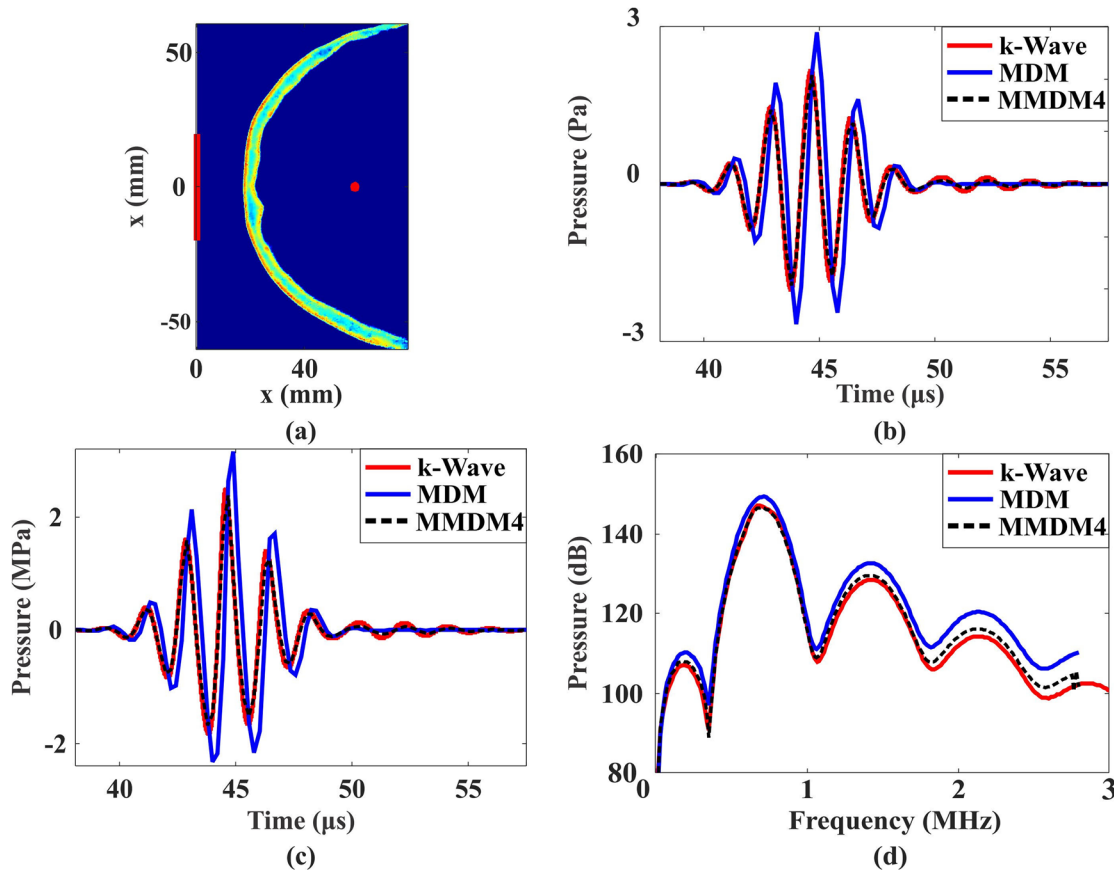


FIG. 4. (Color online) (a) A 2D skull model. The red line on the left indicates the array position and the red dot is the geometrical focus. (b) Waveforms recorded at the geometrical focus of the transducer. The results simulated by *k*-Wave, the MDM, and the MMDM4 are compared when the medium is linear. (c) Time-domain and (d) frequency-domain results at the geometrical focus of the transducer. The results simulated by *k*-Wave, the MDM, and the MMDM4 are compared when the nonlinear effect is considered.

MMDM. The medium is considered to be lossless. The effect of acoustic absorption will be addressed in Sec. IV (the discussion section). The absorbing layer is used to minimize the spatial aliasing error, where γ_{\max} is 0.6 and α is 0.05. We first compare the waveforms recorded at the focus of the transducer, which are plotted in Fig. 4(b). The L2-norm error is 1.0716 for the MDM and 0.1120 for the MMDM4. In contrast to the previous case, the even order reflections are not visible in this situation as they are mixed with the primary transmissive (zeroth-order) wave. The nonlinearity coefficient is 3.6 throughout the entire domain, although, in principle, it can be inhomogeneous in the MDM/MMDM. The pressure magnitude is increased to 1 MPa to enhance the nonlinearity effect. The time-domain and frequency-domain results at the focal point of the transducer are shown in Figs. 4(c) and 4(d). The L2-norm error is 1.0967 for the MDM and 0.1261 for the MMDM4. In this case, the error is reduced by a factor of almost 10 for both linear and nonlinear simulations.

By applying the Fourier transform to the transient results, the pressure field at the frequency of interest can be further obtained. Figure 5 shows the second and third harmonics pressure fields computed by *k*-Wave, the MDM, and the MMDM4. Pressure differences between different

methods are also shown, confirming that the MMDM4 is more accurate than the MDM. The pressure fields at the fundamental frequency can be found in Sec. III B and, therefore, are not shown in Fig. 5.

B. Continuous wave beams

The MMDM is also capable of directly modeling the acoustic field at the frequency of interest¹⁵ since this method is intrinsically a frequency-domain method. It is shown that, compared to transient simulations, in which the acoustic field of a certain frequency needs to be acquired by Fourier transform, directly operating the MDM/MMDM at the frequency of interest is orders of magnitude more computationally efficient. This, however, has only been demonstrated for linear and weakly nonlinear cases, in which the couplings between the fundamental frequency and the harmonics are minimal.¹⁵ In this study, linear wave propagation is assumed and the excitation signal in *k*-Wave is a continuous sinusoidal wave at 700 kHz with an amplitude of 1 Pa. For the same 2D skull case, the absorbing layer in the MDM/MMDM is enabled where γ_{\max} is chosen as 0.5 and α is 0.03. Four sets of results, obtained by *k*-Wave, the MDM, the MMDM, and MMDM4, are plotted in Figs. 6(a)–6(d), respectively. Figures 6(e) and 6(f) show the pressure

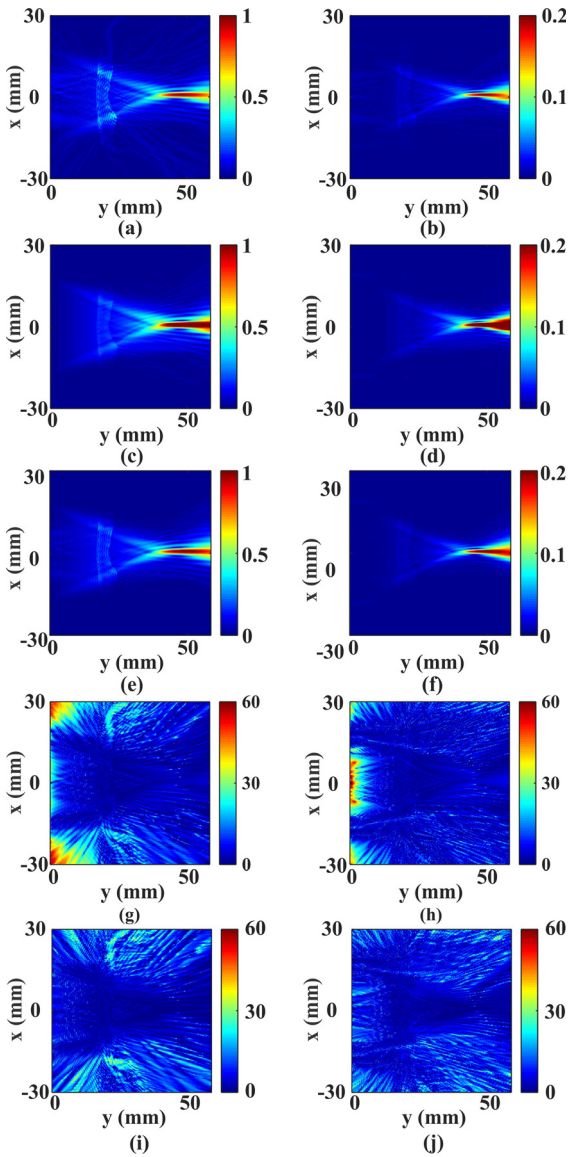


FIG. 5. (Color online) Spatial pressure distributions for the 2D skull nonlinear case. (a) and (b) are the pressure fields at the second and third harmonics generated by *k*-Wave. (c) and (d) are the pressure fields at the second and third harmonics, respectively, generated by the MDM. (e) and (f) are the pressure fields at the second and third harmonics, respectively, generated by the MMDM4. The pressure differences between the MDM and *k*-Wave are shown in (g) and (h), respectively, for the second and third harmonics. The pressure differences between the MMDM4 and *k*-Wave are shown in (i) and (j), respectively, for the second and third harmonics.

difference between the MDM and *k*-Wave and between the MMDM4 and *k*-Wave, respectively. For the region shown in Figs. 6(a)–6(d) (approximately $80 \text{ mm} \times 80 \text{ mm}$), the L2-norm error is 0.3374 for the MDM, 0.2839 for the MMDM, and 0.1717 for the MMDM4, respectively. Axial pressure distributions along $x = 0$ are also compared in Fig. 6(g) between different models.

We have also conducted 3D simulations. A 3D skull-mimicking model is generated as shown in Fig. 7 with a domain size of $42.9 \text{ mm} \times 42.9 \text{ mm} \times 42.9 \text{ mm}$. For the surrounding medium, the speed of sound is 1500 m/s and the density is 1000 kg/m^3 ; for the skull-like medium, the speed

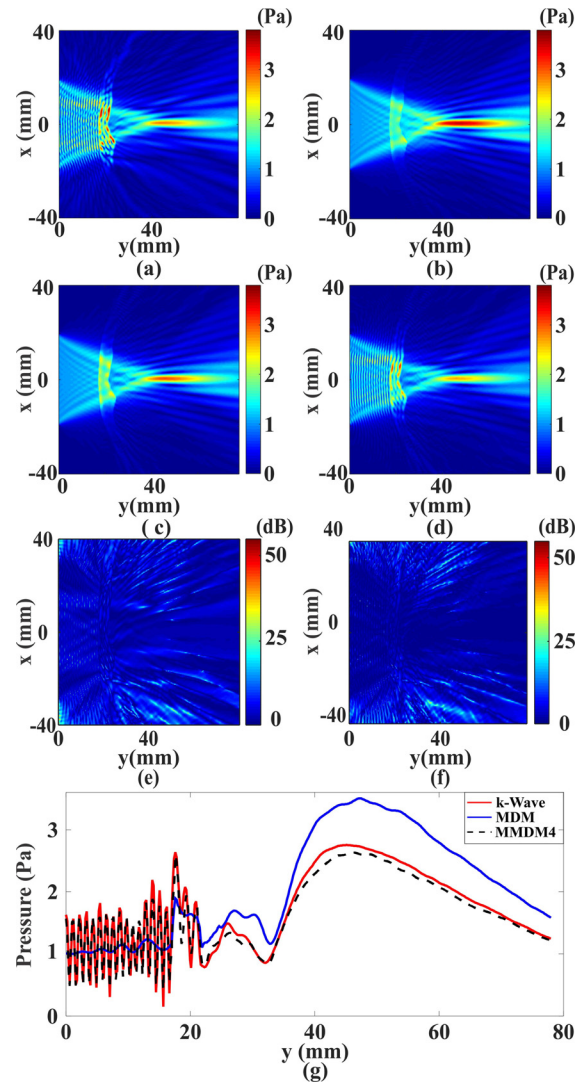


FIG. 6. (Color online) Spatial pressure distributions for the 2D skull case simulated with (a) *k*-Wave, (b) the MDM, (c) the MMDM, and (d) the MMDM4. (e) The difference in dB between the MDM and *k*-Wave. (f) The difference in dB between the MMDM4 and *k*-Wave. (g) Comparison for the axial pressure distribution along $x = 0$.

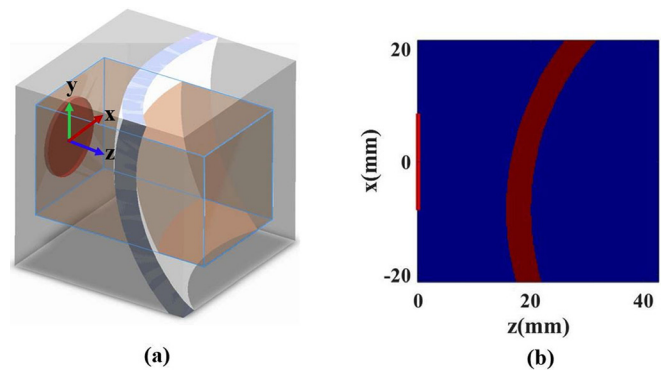


FIG. 7. (Color online) (a) Illustration of the 3D skull-mimicking model. The red disk indicates the size and position of the unfocused transducer. The inner cuboid is the domain where errors are estimated. (b) A cross-sectional view of the 3D heterogeneous medium on the x - z plane ($y = 0$). The red line shows the position of the unfocused transducer.

of sound is 2250 m/s and the density is 1500 kg/m³. An unfocused circular transducer is adopted in this simulation, whose diameter is 17.14 mm. The center frequency and the pressure amplitude are 700 kHz and 1 Pa, respectively. The same spatial resolution is used for all methods and it is 1/10 λ . For the benchmark simulation using *k*-Wave, the time step is 0.0089 μ s (CFL = 0.0938). The absorbing layer in the MDM/MMDM is enabled where γ_{\max} is 0.5 and α is 0.05. Pressure fields on three orthogonal planes are shown in

Fig. 8. The three planes intersect at the natural focal point, i.e., the center point of the near-field distance plane ($z = a^2/\lambda = 34.3$ mm, where a is the transducer radius). Figures 8(a)–8(c) show results from *k*-Wave, Figs. 8(d)–8(f) show results from the MDM, Figs. 8(g)–8(i) are generated by the MMDM, and Figs. 8(j)–8(l) are generated by the MMDM4. Figures 8(m)–8(o) display the pressure differences between *k*-Wave and the MMDM4 in all three planes. The L2-norm errors calculated within a cuboid region highlighted in

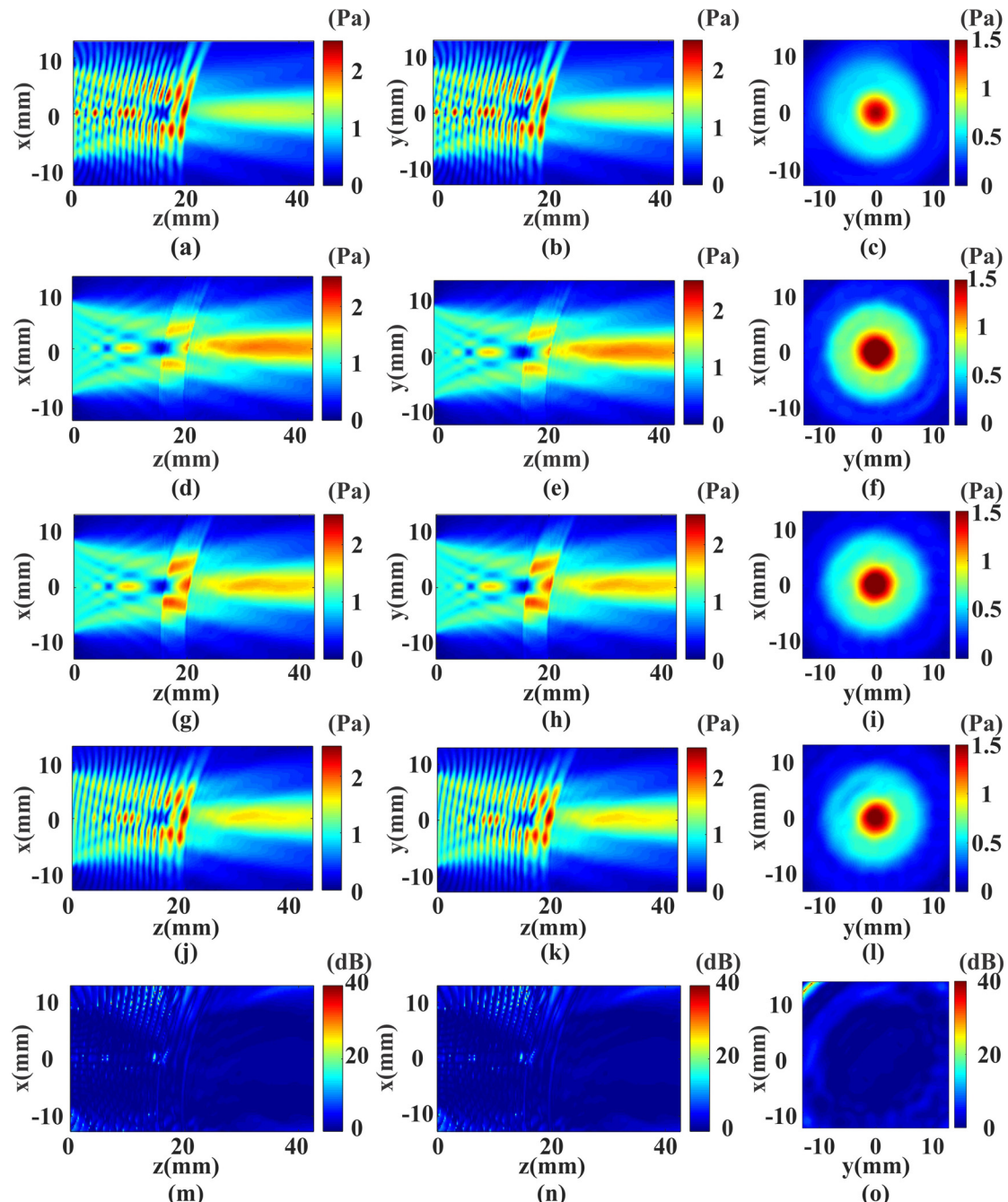


FIG. 8. (Color online) Pressure fields for the 3D model. (a)–(c) are generated by *k*-Wave, (d)–(f) are generated by the MDM, (g)–(i) are generated by the MMDM, and (j)–(l) are generated by the MMDM4. The first column [(a), (d), (g), (j)] displays the pressure field on the x - z plane at $y = 0$. The second column [(b), (e), (h), (k)] displays the pressure field on the y - z plane at $x = 0$. The third column displays the pressure field on the x - y plane at the near field distance. (m)–(o) display the pressure difference between *k*-Wave and the MMDM4.

Fig. 7(a) ($25.5000\text{ mm} \times 25.5000\text{ mm} \times 42.6429\text{ mm}$) are 0.3433 for the MDM, 0.3199 for the MMDM, and 0.1773 for the MMDM4, respectively.

IV. DISCUSSION

We have investigated the accuracy of the MMDM for modeling linear/nonlinear wave propagation in strongly heterogeneous media. It is found that with phase correction, amplitude compensation, as well as the addition of reflections, the MMDM is significantly more accurate than the original MDM for the cases tested in this study. The MMDM, in a way, is similar to the iterative nonlinear contrast source (INCS) method^{7,8} in that both methods aim to solve an integral equation and treat the perturbation to the incident field as a contrast source. These two methods, however, also differ in many important aspects. For instance, the MMDM solves the integral equation using a marching scheme, whereas the INCS method uses iterative approaches (e.g., the Neumann scheme). For 3D (x, y, z) problems, the INCS method operates on four-dimensional (4D) (x, y, z, t) matrices while the MMDM involves 3D (x, y, t) matrices for transient problems or 2D (x, y) matrices for steady-state problems. The INCS method is more accurate in computing the multiple scattering provided that the iterative scheme is robust, whereas for the MMDM, the integral equation does not account for the multiple scattering and it has to be calculated in an *ad hoc* manner, in which the accuracy hinges on 1D approximation, which we will discuss at length below.

Some deviations in terms of the pressure amplitude between the MMDM and *k*-Wave results can be observed in the skull case (e.g., Fig. 4). This is likely due to the fact that the amplitude compensation introduced in the MMDM is based on the 1D assumption, although there is also the possibility that *k*-Wave results are less accurate for a complicated structure like the skull²⁹ given the relatively low spatial resolution used in this instance (limited by the CT scan). This could also explain why the amplitude deviation is less visible in the layered medium case as the layer has a more regular shape and, therefore, the 1D assumption is more applicable and *k*-Wave results are also potentially

more accurate in this case. To confirm this, we investigate a case where the layer is tilted at an angle of 11° instead of being normal to the beam direction [Fig. 9(a)]. The density and speed of sound contrast are kept at 2.0. The time-domain waveforms recorded at the focal point of the transducer are compared in Fig. 9(b). The L2-norm error is 1.6360 for the MDM and 0.4435 for the MMDM4. Here, larger amplitude differences are observed while the phase correction is still robust, although the 1D assumption breaks down. We have also studied the L2-norm errors with different tilt angles. As shown in Fig. 9(c), the error expectedly grows as the title angle increases. While it is not clear how the values of these errors can be generalized to other cases with different ultrasound beams, layer thicknesses, and source-layer distances, the error does become rather significant when the tilt angle increases. It should also be pointed out that at large angles, acoustic wave models become intrinsically unsuitable for modeling transcranial ultrasound due to its inability to consider mode conversion. Another scenario where the 1D assumption could break down is when the wave field is strongly diverging (e.g., a spherical or cylindrical wave). This, however, is less relevant to therapeutic ultrasound and, thus, is not discussed here.

Multiple reflections have been studied as a means to improve the model. Figure 3(b), for example, suggests that the second- and fourth-order reflections can be accurately modeled. Figures 6 and 8 compare the spatial pressure distribution for the skull and skull-mimicking cases, simulated with *k*-Wave, the MDM, the MMDM, and the MMDM4. When reflections are included in the simulation, the accuracy is both visibly and quantitatively improved. For example, Fig. 6(d) indicates that the focal size is more precisely predicted and the interference pattern as a result of waves traveling in opposite directions is clearly exhibited.

The numerical implementation throughout this study is based on MATLAB 2018a (The MathWorks Inc., Natick, MA) on a 64-bit operating system with a 12-core 3.00-GHz Intel Xeon (R) Gold 6136 central processing unit (CPU; Intel Corp., Santa Clara, CA) processor and 192 GB of random access memory (RAM). To simulate transient wave

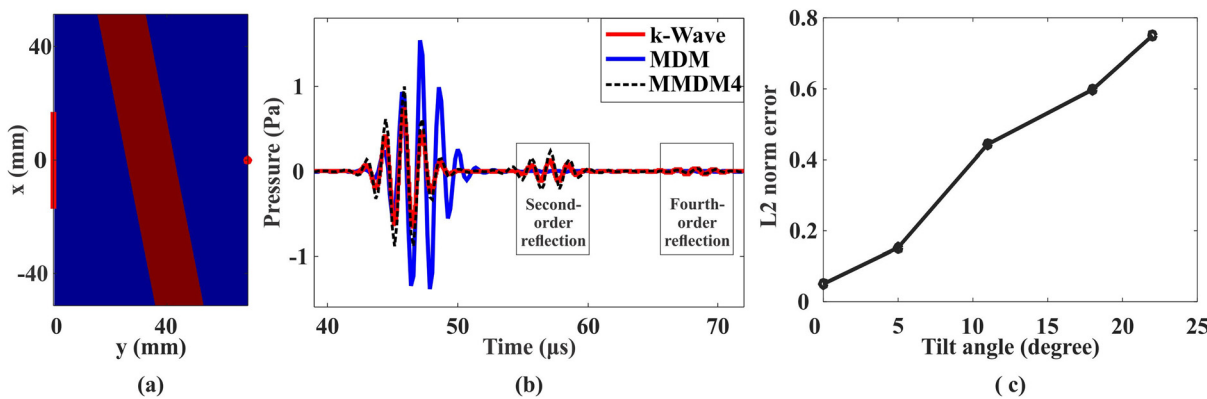


FIG. 9. (Color online) (a) A 2D oblique-layered media. The red line indicates the position of the phased array transducer and the red dot indicates the position of the transducer focus. (b) Comparison of the waveforms at the geometrical focus of the transducer simulated with *k*-Wave, the MDM, and the MMDM4. (c) L2-norm error as a function of the tilt angle.

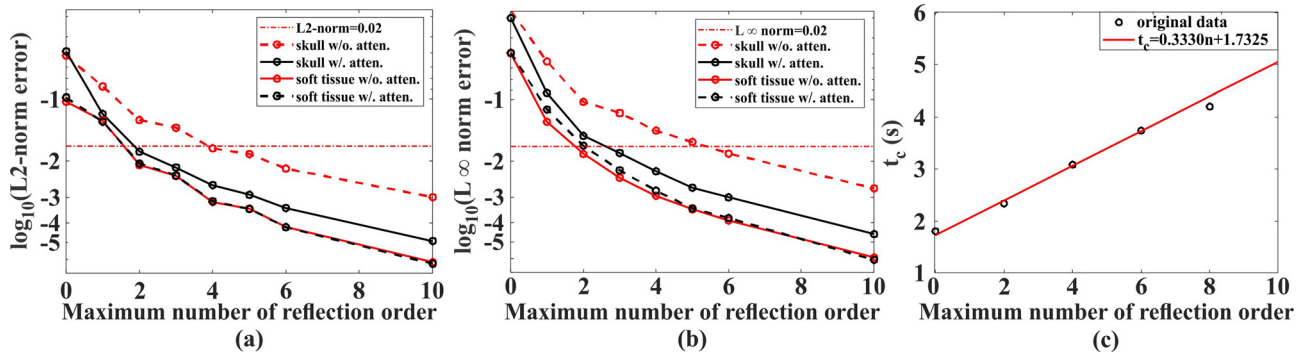


FIG. 10. (Color online) Reflection convergence study of the MMDM for the 2D skull and soft tissue cases with and without attenuation. (a) L2-norm error vs the order of reflection, (b) infinity-norm error vs the order of reflection, and (c) computational time vs the order of reflection for the 2D skull simulation.

propagation using the 2D skull, the MMDM takes about 85 s, the MMDM4 takes about 345 s, and *k*-Wave takes about 650 s, given a computational domain that is about 120 mm \times 60 mm and with the same spatial resolution for all three methods. For generating the results shown in Fig. 6, however, the MMDM only takes about 1.80 s, the MMDM4 takes about 5.7 s and *k*-Wave takes around 1200 s. Even if the CFL number is increased to 0.3 (the default number in *k*-Wave), *k*-Wave would still take a considerably longer time to produce the steady-state result. The fast speed of the MMDM/MMDM4 can be attributed to the fact that this method computes the acoustic field directly at the center frequency,¹⁴ therefore, in this case, reducing a 3D (*x*, *y*, *t*) problem to a 2D (*x*, *y*) problem that can be solved more rapidly with less computer memory. It is important to note that (1) the efficiency comparisons do not consider the fact that the models give different accuracies. While the MMDM will still likely be much faster than *k*-Wave for the steady-state case, the transient modeling may not if we were to compare the two models under the same accuracy; and (2) the MMDM or MDM transient modeling can be potentially faster by applying a time window which moves with the incident field. This will be addressed in our future study, and (3) these comparisons are made using the MATLAB version of *k*-Wave. Optimized c++ and compute unified device architecture (CUDA) versions of *k*-Wave are also available and can significantly reduce computation times.

Although the MMDM is computationally efficient, the computation time inevitably increases when high-order reflections are considered. Thus, it is necessary to conduct a convergence study on multiple reflections: how many reflections are necessary for achieving satisfactory results? To this end, we first examine the steady state results for the 2D skull model with the MMDM. The L2-norm errors are calculated using the MMDM50 result as the benchmark solution and the errors are plotted in Fig. 10(a). The result is considered converged when the L2-norm error is less than 0.02. It can be seen that the result is indeed converging, indicating a less significant role of higher-order reflections. The fourth-order reflection is required for the lossless skull simulation to attain sufficiently accurate results (L2-norm error < 0.02). For a more realistic simulation, absorption,

which can be deduced by the density,³⁰ is added to the skull. The absorption coefficient varies from 0.005 dB cm⁻¹ to 23.45 dB cm⁻¹ (taken from Ref. 31 at 836 kHz). The power law exponent is 2.0 in this case as there is no well-established data on the power law exponent for skulls. The result is seen to converge faster with the consideration of absorption, and the second-order reflection is sufficient to have the error less than 0.02. The results of *k*-Wave are not provided for the lossy skull case because *k*-Wave is less accurate when large absorption values are considered.³² To provide more insight on the convergence of the error with respect to the order of reflection, we have also calculated the relative infinity norm errors, defined as

$$L_{\infty} = \frac{\max(p - p_{\text{benchmark}})}{\max(p_{\text{benchmark}})} \quad (19)$$

These results are shown in Fig. 10(b). It requires third-order reflection for the lossy skull case to make the relative infinity norm error less than 0.02.

Two additional questions naturally arise: is it necessary to apply the corrections for soft tissue where the heterogeneities are relatively weak? Is it necessary to consider multiple reflections in soft tissue? To answer this question, a tissue map is considered as illustrated in Fig. 11(a). The acoustical properties for different tissue parts are listed in Table I. The excitation pressure magnitude is 1 Pa and the center frequency is 700 kHz. The transducer focal length is 49.5 mm and its diameter is 33.2 mm, corresponding to an *F* number of 1.5. The lossless case is first considered. The 2D pressure distributions obtained by *k*-Wave, the MDM, and the MDM2 are shown in Figs. 11(b), 11(c), and 11(d), respectively. The axial pressure distributions along *x* = 0 are shown in Fig. 11(e) for *k*-Wave, the MDM, the MMDM, and the MDM2. The L2-norm error calculated using the whole domain is 0.1432 for the MDM and 0.1403 for the MMDM (the 2D pressure distribution calculated by the MMDM is not shown in this paper). Thus, the corrections in phase and amplitude do not significantly improve the MDM in this case. The L2-norm error, on the other hand, is 0.1181 for the MDM2, indicating that the inclusion of reflections is, in fact, more important than the correction. While these results suggest that it may not be necessary to apply

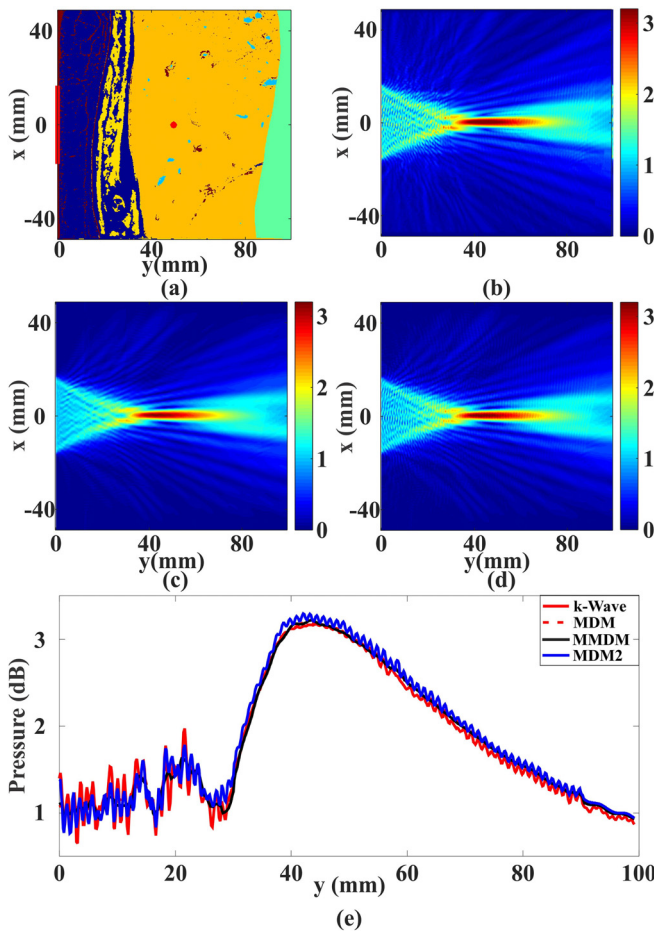


FIG. 11. (Color online) (a) A 2D human tissue map. The superficial layers from the left to the right denote connective tissue (red), fat (dark blue) with embedded connective tissue (red), muscle (yellow), liver (orange), and tissue (green). Blood (light blue) is inside the liver. The red line on the left boundary indicates the array position. The red dot is the geometrical focus. Spatial pressure distributions simulated with (b) *k*-Wave, (c) the MDM, and (d) the MDM2 are shown. (e) Comparison of the axial pressure distributions along the beam axis.

corrections to the MDM for soft tissue, this conclusion should be scrutinized for problems involving considerably larger computational domains since the phase and amplitude errors grow along the wave propagation direction in the MDM. The convergence study for the lossless soft tissue and lossy soft tissue are also carried out, and the results are shown in Figs. 10(a) and 10(b), respectively, with the MMDM50 results as the benchmark. It can be concluded that in this soft tissue case, up to second-order reflection

TABLE II. L2-norm errors for the time-domain results.

	MDM	MMDM4	MDM ^a	MMDM4 ^a
Linear parallel layer	1.2137	0.0509	0.5743	0.0412
Nonlinear parallel layer	1.2234	0.0579	0.5715	0.0695
Linear skull	1.0716	0.1120	0.8201	0.0671
Nonlinear skull	1.0967	0.1261	0.8105	0.0842
Oblique layer (11°)	1.6360	0.4435	0.4208	0.1227

^aThe error is calculated by using only the scattering field.

could be sufficient to obtain converged results (L2-norm error is less than 0.02; infinity norm error is barely above 0.02 in the lossy case, i.e., 0.0208). Please note that the error 0.02 was chosen empirically as the criterion. If a different error were chosen, the conclusion regarding the maximum order of reflection could change. For example, if 0.01 were to be used as the L2-norm error criterion, convergence will require up to the third-order reflection for the lossy skull case. Therefore, ultimately, the reflection should be modeled based on the specific need of the user.

We have also studied the order of convergence p by using the following equation:

$$\text{error} = C \frac{1}{n^q}, \quad (20)$$

where q is the order of convergence, C is the asymptotic constant, and n is the order of the reflection. Through fitting the curves in Fig. 10(a), the convergence order for the skull without attenuation is found to be 2.01, and for the case with attenuation, the convergence order for the skull is 3.5. The convergence order for the soft tissue without attenuation is 4.639 and 4.71 for the case with attenuation. Additionally, the computation time is a linear function of the reflection order n . For example, the computation times for the 2D skull with different n are shown in Fig. 10(c).

Finally, while the previous L2-norm errors are computed using the total acoustic field, we have also calculated the errors using only the scattering field. The scattering is computed by first conducting the simulation using the homogeneous medium (incident field) and, then, using the heterogeneous medium (total field). Subsequently, we calculate the difference between the two results to extract the scattering field. These errors, along with previous ones, are summarized in Tables II and III. One thing to note is that the errors calculated using only the scattering field for the soft tissue are rather large even with multiple scattering

TABLE I. Tissue acoustical properties.

	Nonlinearity coefficient	Speed of sound (m/s)	Density (kg/m ³)	Attenuation coefficient at 1 MHz (dB/cm)	Power law exponent, y
Connective	5.0	1613	1120	1.57	1.1
Fat	5.8	1478	950	0.48	1.1
Muscle	5.5	1547	1050	1.09	1.1
Liver	4.3	1595	1060	0.5	1.2
Blood	4.05	1584	1060	0.2	2.0
Tissue	5.5	1540	1000	0.5	1.1

TABLE III. L2-norm errors for the frequency-domain results.

	MDM	MMDM	MMDM4 for skull and MDM2 for soft tissue
2D skull	0.3374	0.2839	0.1717
Soft tissue	0.1432	0.1403	0.1181
3D skull	0.3433	0.3199	0.1773
2D skull ^a	0.7816	0.6421	0.3622
Soft tissue ^a	0.7568	0.7412	0.6410
3D skull ^a	0.9333	0.8539	0.4525

^aThe error is calculated by using only the scattering field.

taken into consideration, e.g., 0.6410 for the MDM2. This is because the scattering field in this case is rather weak and, therefore, is more susceptible to errors.

V. CONCLUSION

In this paper, phase correction and amplitude compensation are proposed and implemented in the MDM so that the algorithm is more suited to modeling wave propagation in strongly heterogeneous media. The resulting model, i.e., the MMDM, is evaluated by studying four different cases with strong speed of sound and density contrasts. Simulation results show that the MMDM is considerably more accurate in terms of predicting the phase and amplitude of the waveform provided that the ultrasound beam is approximately perpendicular to the phase aberrating layer as demonstrated by Fig. 9(c). It is also shown that reflections can be added to the MMDM to further improve the accuracy of the model. Convergence studies show that the second-order reflection could be sufficient for soft tissue and lossy skull simulations. While the computation time increases with the addition of reflections, the MMDM is still computationally efficient when used to predict the steady-state wave field at specific frequencies of interest. In the future, the MMDM can be coupled with the bioheat transfer equation to estimate temperature elevation in the tissue. Backward propagation can also be investigated for applications such as phase correction and photoacoustic tomography in heterogeneous media.

ACKNOWLEDGMENTS

This work was supported by the U.S. National Institutes of Health (Grant No. R01EB025205).

- ¹A. I. Farrer, S. Almquist, C. R. Dillon, L. A. Neumayer, D. L. Parker, D. A. Christensen, and A. Payne, "Phase aberration simulation study of MRgFUS breast treatments," *Med. Phys.* **43**(3), 1374–1384 (2016).
- ²G. Clement and K. Hynynen, "A non-invasive method for focusing ultrasound through the human skull," *Phys. Med. Biol.* **47**(8), 1219–1236 (2002).
- ³T. Wang and Y. Jing, "Transcranial ultrasound imaging with speed of sound-based phase correction: A numerical study," *Phys. Med. Biol.* **58**(19), 6663 (2013).
- ⁴C. Huang, L. Nie, R. W. Schoonover, Z. Guo, C. O. Schirra, M. A. Anastasio, and L. V. Wang, "Aberration correction for transcranial photoacoustic tomography of primates employing adjunct image data," *J. Biomed. Opt.* **17**(6), 066016 (2012).
- ⁵G. Sandhu, C. Li, O. Roy, S. Schmidt, and N. Duric, "Frequency domain ultrasound waveform tomography: Breast imaging using a ring transducer," *Phys. Med. Biol.* **60**(14), 5381 (2015).

⁶G. F. Pinton, G. E. Trahey, and J. J. Dahl, "Sources of image degradation in fundamental and harmonic ultrasound imaging using nonlinear, full-wave simulations," *IEEE Trans. Ultrason. Ferroelectr. Freq. Control* **58**(4), 754–765 (2011).

⁷L. Demi, K. v. Dongen, and M. Verweij, "A contrast source method for nonlinear acoustic wave fields in media with spatially inhomogeneous attenuation," *J. Acoust. Soc. Am.* **129**(3), 1221–1230 (2011).

⁸L. Demi, M. D. Verweij, and K. W. van Dongen, "Modeling three-dimensional nonlinear acoustic wave fields in media with spatially varying coefficient of nonlinearity, attenuation and speed of sound," in *IEEE International Ultrasonics Symposium* (2012), pp. 519–522.

⁹B. E. Treeby, J. Jaros, A. P. Rendell, and B. Cox, "Modeling nonlinear ultrasound propagation in heterogeneous media with power law absorption using a *k*-space pseudospectral method," *J. Acoust. Soc. Am.* **131**(6), 4324–4336 (2012).

¹⁰Y. Jing, T. Wang, and G. T. Clement, "A *k*-space method for moderately nonlinear wave propagation," *IEEE Trans. Ultrason. Ferroelectr. Freq. Control* **59**(8), 1664–1673 (2012).

¹¹G. F. Pinton, J. Dahl, S. Rosenzweig, and G. E. Trahey, "A heterogeneous nonlinear attenuating full-wave model of ultrasound," *IEEE Trans. Ultrason. Ferroelectr. Freq. Control* **56**(3), 474–488 (2009).

¹²G. Clement and K. Hynynen, "Field characterization of therapeutic ultrasound phased arrays through forward and backward planar projection," *J. Acoust. Soc. Am.* **108**(1), 441–446 (2000).

¹³U. Vyas and D. Christensen, "Ultrasound beam simulations in inhomogeneous tissue geometries using the hybrid angular spectrum method," *IEEE Trans. Ultrason. Ferroelectr. Freq. Control* **59**(6), 1093–1100 (2012).

¹⁴J. Gu and Y. Jing, "Numerical modeling of ultrasound propagation in weakly heterogeneous media using a mixed domain method," *IEEE Trans. Ultrason. Ferroelectr. Freq. Control* **65**(7), 1258–1267 (2018).

¹⁵J. Gu and Y. Jing, "Simulation of the second harmonic ultrasound field in heterogeneous soft tissue using a mixed domain method," *IEEE Trans. Ultrason. Ferroelectr. Freq. Control* **66**(4), 669–675 (2019).

¹⁶J. Gu and Y. Jing, "Modeling of wave propagation for medical ultrasound: A review," *IEEE Trans. Ultrason. Ferroelectr. Freq. Control* **62**(11), 1979–1992 (2015).

¹⁷N. Lipsman, T. G. Mainprize, M. L. Schwartz, K. Hynynen, and A. M. Lozano, "Intracranial applications of magnetic resonance-guided focused ultrasound," *Neurotherapeutics* **11**(3), 593–605 (2014).

¹⁸N. McDannold, G. T. Clement, P. Black, F. Jolesz, and K. Hynynen, "Transcranial magnetic resonance imaging-guided focused ultrasound surgery of brain tumors: Initial findings in 3 patients," *Neurosurgery* **66**(2), 323–332 (2010).

¹⁹J. Kubanek, "Neuromodulation with transcranial focused ultrasound," *Neurosurg. Focus* **44**(2), E14 (2018).

²⁰B. E. Treeby and B. T. Cox, "k-Wave: MATLAB toolbox for the simulation and reconstruction of photoacoustic wave fields," *J. Biomed. Opt.* **15**(2), 021314 (2010).

²¹S. Pourjavid and O. J. Tretiak, "Numerical solution of the direct scattering problem through the transformed acoustical wave equation," *J. Acoust. Soc. Am.* **91**(2), 639–645 (1992).

²²T. D. Mast, L. P. Souriau, D.-L. Liu, M. Tabei, A. I. Nachman, and R. C. Waag, "A *k*-space method for large-scale models of wave propagation in tissue," *IEEE Trans. Ultrason. Ferroelectr. Freq. Control* **48**(2), 341–354 (2001).

²³P. Wu, R. KKazys, and T. Stepinski, "Analysis of the numerically implemented angular spectrum approach based on the evaluation of two-dimensional acoustic fields. Part II. Characteristics as a function of angular range," *J. Acoust. Soc. Am.* **99**, 1349–1359 (1996).

²⁴Y. Jing, "On the use of an absorption layer for the angular spectrum approach (L)," *J. Acoust. Soc. Am.* **131**(2), 999–1002 (2012).

²⁵Y. Jing, M. Tao, and G. T. Clement, "Evaluation of a wave-vector-frequency-domain method for nonlinear wave propagation," *J. Acoust. Soc. Am.* **129**(1), 32–46 (2011).

²⁶Y. Jing, M. Tao, and J. Cannata, "An improved wave-vector frequency-domain method for nonlinear wave modeling," *IEEE Trans. Ultrason. Ferroelectr. Freq. Control* **61**(3), 515–524 (2014).

- ²⁷X. Zhao and R. J. McGough, "Time-domain comparisons of power law attenuation in causal and noncausal time-fractional wave equations," *J. Acoust. Soc. Am.* **139**(5), 3021–3031 (2016).
- ²⁸L. E. Kinsler, A. R. Frey, A. B. Coppens, and J. V. Sanders, "Fundamentals of acoustics," in *Fundamentals of Acoustics*, 4th ed. (Wiley-VCH, Hoboken, NJ, 1999), 560 pp.
- ²⁹J. L. Robertson, B. T. Cox, J. Jaros, and B. E. Treeby, "Accurate simulation of transcranial ultrasound propagation for ultrasonic neuromodulation and stimulation," *J. Acoust. Soc. Am.* **141**(3), 1726–1738 (2017).
- ³⁰Y. Jing, F. C. Meral, and G. T. Clement, "Time-reversal transcranial ultrasound beam focusing using a k -space method," *Phys. Med. Biol.* **57**(4), 901 (2012).
- ³¹S. Pichardo, V. W. Sin, and K. Hyynnen, "Multi-frequency characterization of the speed of sound and attenuation coefficient for longitudinal transmission of freshly excised human skulls," *Phys. Med. Biol.* **56**(1), 219 (2010).
- ³²B. E. Treeby and B. Cox, "Modeling power law absorption and dispersion in viscoelastic solids using a split-field and the fractional Laplacian," *J. Acoust. Soc. Am.* **136**(4), 1499–1510 (2014).